Non-Hermitian $\mathbb{Z}_4$ skin effect protected by glide symmetry

Sho Ishikawa[1] and Tsuneya Yoshida[1,2]
[1]*Department of Physics, Kyoto University, Kyoto 606-8502, Japan*
[2]*Institute for Theoretical Physics, ETH Zurich, 8093 Zurich, Switzerland*

(Received 11 July 2024; revised 18 August 2024; accepted 20 August 2024; published 3 September 2024)

Although nonsymmorphic symmetry protects $\mathbb{Z}_4$ topology for Hermitian systems, non-Hermitian topological phenomena induced by such a unique topological structure remain elusive. In this paper, we elucidate that systems with glide symmetry exhibit non-Hermitian skin effects (NHSE) characterized by $\mathbb{Z}_4$ topology. Specifically, numerically analyzing a two-dimensional toy model, we demonstrate that the $\mathbb{Z}_4$ topology induces the NHSE when the topological invariant takes $\nu = 1$ and 2. Furthermore, our numerical analysis demonstrates that the NHSE is destroyed by perturbations preserving the relevant symmetry when the $\mathbb{Z}_4$ invariant takes $\nu = 4$.

DOI: 10.1103/PhysRevB.110.115301

I. INTRODUCTION

Topology of wave functions in insulators and superconductors is one of the central issues in condensed-matter physics because of gapless boundary states induced by topology in the bulk [1–6]. The integer quantum Hall system [7–13] is an example of topological insulators without symmetry where the chiral edge mode results in quantized Hall conductance with high accuracy. Topological structures are enriched by time-reversal symmetry, particle-hole symmetry, and chiral symmetry [14–17] as systematically clarified by the tenfold way classification [18–21]; three (two) symmetry classes allow $\mathbb{Z}$ ($\mathbb{Z}_2$) topology in each case of spatial dimensions. Topological structures are further enriched by crystalline symmetry [22–28]. In particular, unique topological structures may exist under nonsymmorphic symmetry [29–41]. For instance, $\mathbb{Z}_4$ topology is allowed under glide symmetry which is described by a product of reflection and the half-translation. This unique $\mathbb{Z}_4$ topology results in distinctive surface states analogous to a Möbius strip [32].

The notion of topology is further extended to non-Hermitian systems, which elucidated that non-Hermiticity induces novel topological phenomena without Hermitian counterparts [42–58]. A representative example is the non-Hermitian skin effect (NHSE), which is the extreme sensitivity of eigenvalues and eigenstates to the boundary conditions due to point-gap topology [59–65]. Because of nontrivial point-gap topology, most of all eigenmodes are localized around only one of the edges which are known as skin modes [62]. While the above NHSE is reported for systems with no symmetry, symmetry-protected NHSEs are also reported for systems with time-reversal symmetry [62] or reflection symmetry [66]. The NHSEs are reported for a variety of classical systems [67–81] as well as quantum systems [82–86].

The above two progresses imply the potential presence of exotic non-Hermitian phenomena under nonsymmorphic symmetry. Although several works have explored the non-Hermitian topology under nonsymmorphic symmetry [87–89], non-Hermitian topological phenomena induced by $\mathbb{Z}_4$ topology remain elusive.

In this paper, we numerically demonstrate the emergence of the NHSE induced by $\mathbb{Z}_4$ topology in systems with glide symmetry. Specifically, we elucidate that the NHSE emerges in a two-dimensional toy model when the $\mathbb{Z}_4$ topological invariant takes $\nu = 1$ and 2. The NHSE characterized by $\nu = 2$ appears only for boundaries where glide symmetry is closed. In addition, one-dimensional topology is trivial for the toy model of $\nu = 2$. Furthermore, we observe that the NHSE is destroyed by perturbations preserving the relevant symmetry for $\nu = 4$, which indicates that the NHSE is induced by $\mathbb{Z}_4$ topology. The above results elucidate the emergence of the non-Hermitian $\mathbb{Z}_4$ skin effect protected by glide symmetry.

The rest of this paper is organized as follows. In Sec. II, we discuss the $\mathbb{Z}_4$ invariant in non-Hermitian systems with glide symmetry. In Sec. III, we observe the emergence of NHSE characterized by the $\mathbb{Z}_4$ invariant. Section IV provides a brief summary of our work. Appendices are devoted to symmetry of doubled Hermitian Hamiltonians, their edge modes, and one-dimensional topology.

II. $\mathbb{Z}_4$ TOPOLOGICAL INVARIANT AND RELEVANT SYMMETRY

We consider a two-dimensional non-Hermitian Hamiltonian with the following symmetry (TRS†):

$$\mathcal{T}H^T(\boldsymbol{k})\mathcal{T}^{-1} = H(-\boldsymbol{k}), \tag{1}$$

where $\mathcal{T}$ is a unitary matrix satisfying $\mathcal{T}\mathcal{T}^* = -1$. This non-Hermitian Hamiltonian belongs to [48] class AII†. Furthermore, we add glide symmetry for the non-Hermitian system:

$$\mathcal{G}(k_x)H(\boldsymbol{k})\mathcal{G}^{-1}(k_x) = H^\dagger(\boldsymbol{k}), \tag{2}$$

where $\mathcal{G}(k_x)$ is a glide operator satisfying $\mathcal{G}^2(k_x) = -e^{-ik_x}$ and $\mathcal{T}\mathcal{G}^*(k_x)\mathcal{T}^{-1} = \mathcal{G}(-k_x)$.

In the presence of symmetry constraints [Eqs. (1) and (2)], the non-Hermitian topology is characterized by a $\mathbb{Z}_4$ topological invariant. In order to see this, we consider the following doubled Hermitian Hamiltonian with a reference energy

$E_{\rm ref} \in \mathbb{C}$:

$$\tilde{H}(E_{\rm ref}) = \begin{pmatrix} 0 & H - E_{\rm ref}\mathbb{1} \\ H^\dagger - E_{\rm ref}^*\mathbb{1} & 0 \end{pmatrix}, \tag{3}$$

where $\mathbb{1}$ is the identity matrix. This Hermitian Hamiltonian belongs to class DIII and has glide symmetry (for more details see Appendix A 1). The above Hamiltonian $\tilde{H}(E_{\rm ref})$ is known to be characterized by the following $\mathbb{Z}_4$ invariant [32], ν:

$$\nu \equiv \frac{2i}{\pi}\int_{-\pi}^{\pi} dk_y \,{\rm tr}\,\mathcal{A}_+^I(k_x=\pi,k_y) - \frac{i}{\pi}\int_0^{\pi} dk_x \int_{-\pi}^{\pi} dk_y \,{\rm tr}\,\mathcal{F}_+(k_x,k_y) \pmod 4, \tag{4}$$

where $\mathcal{A}_+$ and $\mathcal{F}_+$ are respectively the Berry connection and the Berry curvature for occupied states of $\tilde{H}(E_{\rm ref})$ in the plus-eigensector of the glide operator $G(k_x)$ [for the explicit definition of $G(k_x)$, see Eq. (A5) in Appendix A 1] with eigenvalues $g_\pm(k_x) = \pm ie^{-ik_x/2}$. The superscript I denotes one of the Kramers pair on the one-dimensional subspace specified by $k_x = \pi$ where the time-reversal operation is closed for the plus-eigensector.

III. NON-HERMITIAN SKIN EFFECT CHARACTERIZED BY THE $\mathbb{Z}_4$ TOPOLOGICAL INVARIANT

We numerically elucidate the emergence of the NHSE induced by $\mathbb{Z}_4$ topology under glide symmetry. Specifically, our numerical analysis demonstrates the emergence of an NHSE for $\nu = 1$ and 2. Such an NHSE is destroyed by perturbations preserving the relevant symmetry for $\nu = 4$.

A. NHSE for $\nu = 1$

To investigate the system for $\nu = 1$, we consider the following Hamiltonian:

$$H_1(k_x,k_y) \equiv [m\eta_0 - t\{(1+\cos k_x)\eta_x - \sin k_x\eta_y\}]\rho_0 + it_{\rm sp}[\sin k_x\eta_x - (1-\cos k_x)\eta_y]\rho_z - i2t_{\rm sp}\sin k_y\eta_0\rho_y. \tag{5}$$

Here, m, t, $t_{\rm sp}$, and α are real numbers. Pauli matrices are denoted by η_i and ρ_i ($i = x, y$, and z). Identity matrices are denoted by η_0 and ρ_0. Time-reversal and glide operators are written as $\mathcal{T} = -\eta_0\rho_y$ and $\mathcal{G}(k_x) = i\left(\begin{smallmatrix} 0 & 1 \\ e^{-ik_x} & 0 \end{smallmatrix}\right)_\eta \rho_x$.

This model is obtained from a Bogoliubov–de Gennes (BdG) Hamiltonian of class DIII of Hermitian systems (see Appendix A 2). Employing a numerical method of the discretized Brillouin zone [90–92], we can see that the $\mathbb{Z}_4$ invariant takes $\nu = 1$ for $-4 < m < 4$ and $(t, t_{\rm sp}) = (1, 0.8)$ [see Fig. 1(a)]. This fact is consistent with the presence of helical edge modes of the doubled Hermitian Hamiltonian (see Appendix B).

We numerically analyze the energy spectrum and right eigenstates by changing boundary conditions. By xOBC (yOBC), we denote open boundary conditions in the x (y) direction. By xPBC (yPBC), we denote periodic boundary conditions in the x (y) direction. We set the parameter m to 3 where the $\mathbb{Z}_4$ invariant takes $\nu = 1$ [see Fig. 1(a)]. Unless otherwise noted, periodic boundary conditions are imposed in the x direction (i.e., xPBC).

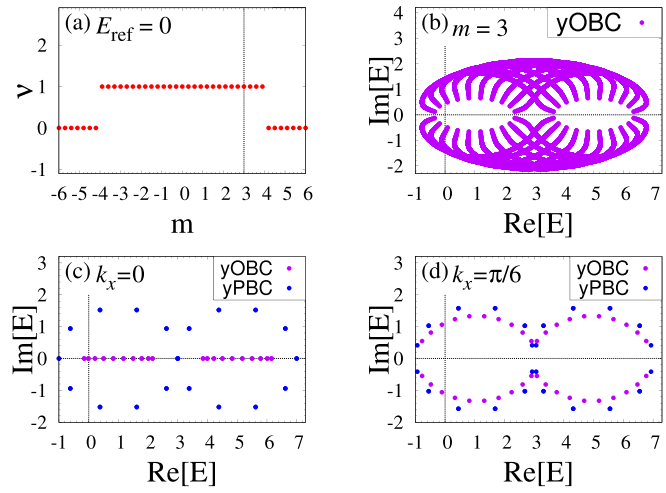

FIG. 1. (a) The $\mathbb{Z}_4$ invariant of H_1 [Eq. (5)] as a function of m. The vertical dotted line denotes $m = 3$. (b) Energy spectra of H_1 [Eq. (5)] under yOBC for $k_x = 2\pi n/10^3$ ($n = 1, \ldots, 10^3 - 1$). The more detailed data obtained for $k_x = 2\pi n/10^4$ ($n = 1, \ldots, 10^4 - 1$) are essentially the same as the data in panel (b). (c) [panel (d)] The energy spectra for $m = 3$ and $k_x = 0$ [$k_x = \pi/6$]. Data denoted by purple (blue) dots are obtained under yOBC (yPBC). These data are obtained for $(t, t_{\rm sp}) = (1, 0.8)$. Panel (a) is obtained from the Bloch Hamiltonian $H_1(k_x, k_y)$. Panels (b), (c), and (d) are obtained by supposing that $L = 10$ unit cells are aligned in the y direction.

The energy spectra are plotted in Figs. 1(b)–1(d). For $k_x = 0$, the spectrum under yOBC is real while the spectrum under yPBC becomes complex. However, for $k_x \neq 0$, the spectrum becomes complex for both cases of yOBC and yPBC.

The right eigenstates are plotted in Fig. 2. For $k_x = 0$, skin modes emerge around both edges. Namely, eigenstates under yOBC are localized at both ends of the system [Fig. 2(a)] while eigenstates under yPBC are delocalized [Fig. 2(b)]. However, for $k_x \neq 0$, eigenstates under yOBC are delocalized, which is similar to the case of yPBC [see Figs. 2(c) and 2(d)].

To obtain these data, the perturbation [93]

$$H_{1,\rm ptb} = -i\beta\eta_0\rho_x, \tag{6}$$

with a small real number β, is added to lift degeneracy by breaking TRS†. With the above results, we can conclude that the NHSE is observed for the Hamiltonian defined in Eq. (5) where the $\mathbb{Z}_4$ invariant takes $\nu = 1$.

B. NHSE for $\nu = 2$

To investigate the system for $\nu = 2$, we consider the following Hamiltonian:

$$H_2(k_x,k_y) \equiv (m - t\cos k_y)\eta_0\rho_0 + i\kappa\sin(k_x/2)[\cos(k_x/2)\eta_x + \sin(k_x/2)\eta_y]\rho_y + i\Delta\sin k_y\eta_0\rho_z - i2\alpha\sin k_y\eta_z\rho_x. \tag{7}$$

Here, κ and Δ are real numbers. Time-reversal and glide operators are written as $\mathcal{T} = -\eta_0\rho_y$ and $\mathcal{G}(k_x) = i\left(\begin{smallmatrix} 0 & e^{-ik_x} \\ 1 & 0 \end{smallmatrix}\right)_\eta \rho_x$. This model is obtained from a BdG Hamiltonian of class DIII

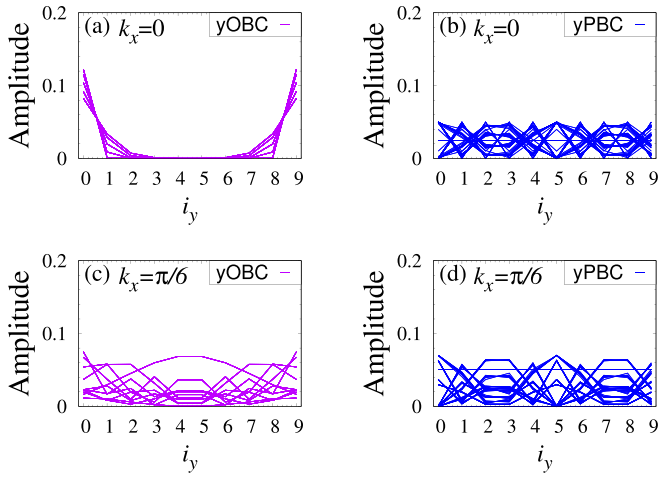

FIG. 2. (a) [panel (b)] Amplitude of right eigenstates of H_1 [see Eq. (5)] under yOBC [yPBC] for $k_x = 0$. (c) [panel (d)] Amplitude of the right eigenstates under yOBC [yPBC] for $k_x = \pi/6$. Unit cells specified by $i_y = 0, 1, \ldots, L-1$ are aligned in the y direction. The amplitude is defined as $|\langle i_y|\Psi_{nR}\rangle|^2$, where $|\Psi_{nR}\rangle$ are the right eigenstates of the Hamiltonian (i.e., $H_1|\Psi_{nR}\rangle = E_n|\Psi_{nR}\rangle$). These data are obtained for $(L, m, t, t_{\rm sp}) = (10, 3, 1, 0.8)$. We have introduced a perturbation [93] [Eq. (6)] with $\beta = 10^{-12}$.

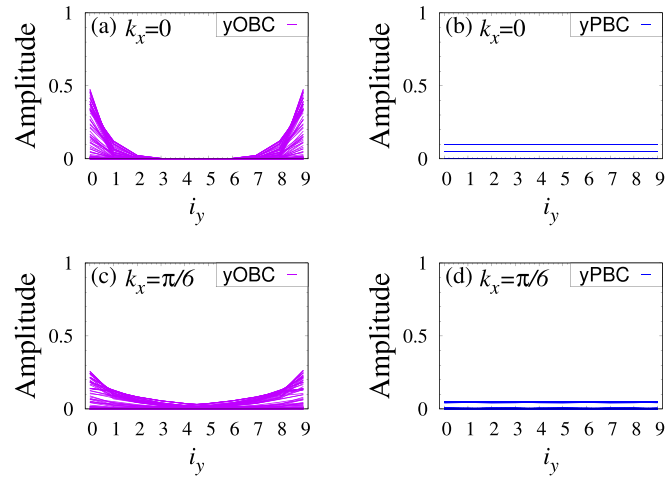

FIG. 4. (a) [panel (b)] Amplitude of right eigenstates of H_2 [see Eq. (7)] under yOBC [yPBC] for $k_x = 0$. (c) [panel (d)] Amplitude of the right eigenstates under yOBC [yPBC] for $k_x = \pi/6$. Unit cells specified by $i_y = 0, 1, \ldots, L-1$ are aligned in the y direction. The amplitude is defined as $|\langle i_y|\Psi_{nR}\rangle|^2$, where $|\Psi_{nR}\rangle$ are the right eigenstates (i.e., $H_2|\Psi_{nR}\rangle = E_n|\Psi_{nR}\rangle$). These data are obtained for $(L, m, t, \kappa, \Delta, \alpha) = (10, 0, 1, 0.2, 0.8, 0.1)$. We have introduced a perturbation [93] [Eq. (8)] with $\beta = 10^{-12}$.

of Hermitian systems (for more details, see Appendices A 2 and B). The $\mathbb{Z}_4$ invariant takes $\nu = 2$ for $-0.8 \leqslant m \leqslant 0.8$ and $(t, \kappa, \Delta, \alpha) = (1, 0.2, 0.8, 0.1)$ [see Fig. 3(a)].

We numerically analyze the energy spectrum and right eigenstates in a way similar to that used in the previous case.

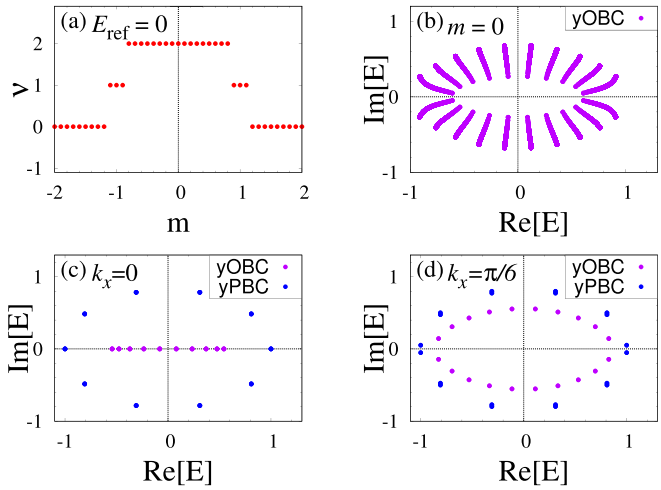

FIG. 3. (a) The $\mathbb{Z}_4$ invariant of H_2 [Eq. (7)] as a function of m. The vertical dotted line denotes $m = 0$. (b) Energy spectra of H_2 [Eq. (7)] under yOBC for $k_x = 2\pi n/10^3$ $(n = 1, \ldots, 10^3 - 1)$. The more detailed data obtained for $k_x = 2\pi n/10^4$ $(n = 1, \ldots, 10^4 - 1)$ are essentially the same data as in panel (b). (c) [panel (d)] The energy spectra for $m = 0$ and $k_x = 0$ [$k_x = \pi/6$]. Data denoted by purple (blue) dots are obtained under yOBC (yPBC). These data are obtained for $(t, \kappa, \Delta, \alpha) = (1, 0.2, 0.8, 0.1)$. Panel (a) is obtained from the Bloch Hamiltonian $H_2(k_x, k_y)$. Panels (b), (c), and (d) are obtained by supposing that $L = 10$ unit cells are aligned in the y direction.

We set the parameter m to 0 where the $\mathbb{Z}_4$ invariant takes $\nu = 2$ [see Fig. 3(a)].

The energy spectra are plotted in Figs. 3(b)–3(d). For $k_x = 0$, the spectrum under yOBC is real while the spectrum under yPBC becomes complex. However, for $k_x \neq 0$, the spectrum becomes complex for both cases of yOBC and yPBC.

The right eigenstates are plotted in Fig. 4. For $k_x = 0$, skin modes emerge around both edges. Namely, eigenstates under yOBC are localized at both ends of the system [Fig. 4(a)] while eigenstates under yPBC are delocalized [Fig. 4(b)]. In contrast, for $k_x \neq 0$, eigenstates under yOBC are delocalized, which is similar to the case of yPBC [see Figs. 4(c) and 4(d)]. To obtain these data, the perturbation [93]

$$H_{2,\rm ptb} = -i\beta\eta_0\rho_x, \tag{8}$$

with a small real number β, is added to lift degeneracy by breaking TRS†.

With the above results, we can conclude that the NHSE is observed for the Hamiltonian defined in Eq. (7), where the $\mathbb{Z}_4$ invariant takes $\nu = 2$.

Here, one may consider that the above NHSE is induced by one-dimensional topology of class AII†. We note, however, that the corresponding topological invariant takes 0 for this model as discussed in Appendix C. We also note that the NHSE disappears when we impose xOBC and yPBC where the glide symmetry is not closed (see Appendix D).

C. NHSE destroyed by perturbations for $\nu = 4$

Stacking two copies of H_2 [Eq. (7)] yields a bilayer system where the $\mathbb{Z}_4$ invariant takes $\nu = 4$. Introducing a coupling between the layers destroys the NHSE while preserving the relevant symmetry, which demonstrates that the NHSE observed in Sec. III B is induced by $\mathbb{Z}_4$ topology.

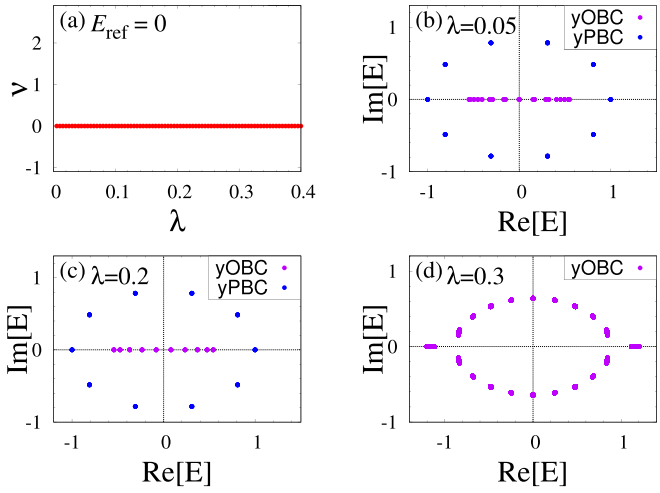

FIG. 5. (a) The $\mathbb{Z}_4$ invariant of H_4 [Eq. (9)] as a function of λ. (b) [panel (c)] Energy spectra of H_4 [Eq. (9)] for $\lambda = 0.05$ [0.2] and $k_x = 0.50536050426$ [π]. Data denoted by purple (blue) dots are obtained under yOBC (yPBC). (d) The energy spectra under yOBC for $k_x = 2\pi n/10^3$ ($n = 0, \ldots, 10^3 - 1$). The more detailed data obtained for $k_x = 2\pi n/10^4$ ($n = 0, \ldots, 10^4 - 1$) are essentially the same as the data in panel (d). These data are obtained for $(m, t, \kappa, \Delta, \alpha) = (0, 1, 0.2, 0.8, 0.1)$. Panel (a) is obtained from the Bloch Hamiltonian $H_4(k_x, k_y)$. Panels (b), (c), and (d) are obtained by supposing that $L = 10$ unit cells are aligned in the y direction.

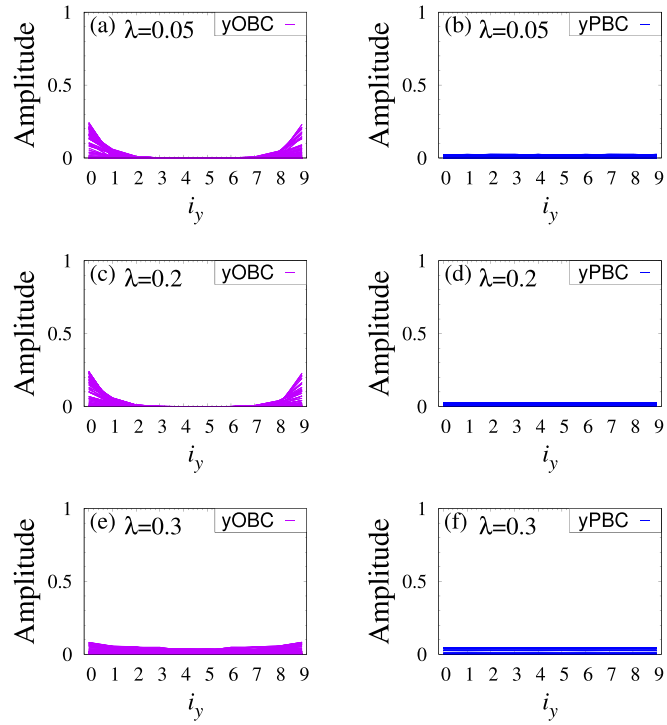

FIG. 6. Amplitude of right eigenstates of H_4 [see Eq. (9)]. Panels (a), (c), and (e) [panels (b), (d), and (f)] are obtained under yOBC [yPBC]. Panels (a) and (b) are obtained for $\lambda = 0.05$. Panels (c) and (d) are obtained for $\lambda = 0.2$. Panels (e) and (f) are obtained for $\lambda = 0.3$. Unit cells specified by $i_y = 0, 1, \ldots, L-1$ are aligned in the y direction. For $\lambda = 0.3$, the data obtained for other wave numbers are essentially the same as the data in panel (e) [panel (f)]. Amplitude is defined as $|\langle i_y|\Psi_{nR}\rangle|^2$, where $|\Psi_{nR}\rangle$ are right eigenstates (i.e., $H_4|\Psi_{nR}\rangle = E_n|\Psi_{nR}\rangle$). These data are obtained under xPBC and for $(L, m, t, \kappa, \Delta, \alpha) = (10, 0, 1, 0.2, 0.8, 0.1)$. We have introduced a perturbation [93] [Eq. (10)] with $\beta = 10^{-12}$.

The above destruction of the NHSE is observed in the following Hamiltonian:

$$H_4(k_x, k_y) = H_2(k_x, k_y)\zeta_0 + \lambda\eta_0\rho_x\zeta_y. \tag{9}$$

Here, λ is a real positive number. Pauli matrices and the identity matrix are denoted by ζ_i ($i = x$, y, and z) and ζ_0, respectively. Time-reversal and glide operators are written as $\mathcal{T} = -\eta_0\rho_y\zeta_0$ and $\mathcal{G}(k_x) = i\begin{pmatrix}0 & e^{-ik_x}\\ 1 & 0\end{pmatrix}_\eta\rho_x\zeta_0$. The second term preserves glide symmetry, $\mathcal{G}(k_x)\lambda\eta_0\rho_x\zeta_y\mathcal{G}^{-1}(k_x) = \lambda\eta_0\rho_x\zeta_y$. As shown in Fig. 5(a), the $\mathbb{Z}_4$ invariant takes $\nu = 0$ for this model.

The energy spectrum is plotted in Figs. 5(b)–5(d). For $\lambda = 0.05$ and 0.2, the spectra under yOBC are real while the spectra under yPBC become complex when k_x takes a specific value. However, for $\lambda = 0.3$, the sensitivity of eigenvalues to boundary conditions is not observed; the spectrum under yOBC becomes complex for arbitrary k_x, which is similar to the case of yPBC.

The right eigenstates are plotted in Fig. 6. For $\lambda = 0.05$ and 0.2, the eigenstates under yOBC are localized at both ends of the system at a specific value of k_x [see Figs. 6(a) and 6(c)] while the eigenstates under yPBC are delocalized [see Figs. 6(b) and 6(d)]. However, for $\lambda = 0.3$, the above localized modes are not observed; the eigenstates under yOBC are delocalized, which is similar to the case of PBC [see Figs. 6(e) and 6(f)]. To obtain these data, the perturbation [93]

$$H_{4,\rm ptb} = -i\beta\eta_0\rho_x\zeta_0, \tag{10}$$

with a small real number β, is added to lift degeneracy by breaking TRS†.

The above results demonstrate that when the $\mathbb{Z}_4$ invariant takes $\nu = 4$, the NHSE is destroyed by perturbations preserving the time-reversal symmetry and the glide symmetry. This fact supports that $\mathbb{Z}_4$ topology induces the NHSEs observed for Hamiltonians defined in Eqs. (5) and (7).

In this section, we have numerically demonstrated that systems with $\nu = 1$ and 2 exhibit NHSEs while the NHSE is destroyed by perturbations preserving the relevant symmetry for $\nu = 4$. We consider that the NHSE emerges for a system with $\nu = 3$ because flipping the sign of the third term of Eq. (5), $[-i2t_{\rm sp}\sin k_y \to i2t_{\rm sp}\sin k_y]$, yields the system with $\nu = -1$ [$= 3$ (mod4)] which exhibits the NHSE. Putting the above results together, we end up with the emergence of non-Hermitian $\mathbb{Z}_4$ skin effects protected by glide symmetry.

IV. SUMMARY

In this paper, we have elucidated that $\mathbb{Z}_4$ topology with glide symmetry induces NHSEs. Specifically, we have numerically analyzed two-dimensional toy models characterized by the $\mathbb{Z}_4$ invariant ν under glide symmetry. Our numerical analysis has clarified that systems with $\nu = 1$ and 2 exhibit the NHSE. The NHSE for $\nu = 2$ is observed only on boundaries

where the glide symmetry is closed. In addition, the one-dimensional subsystem at $k_x = 0$ is trivial for the toy model of $\nu = 2$ [Eq. (7)]. Furthermore, we have observed that the NHSE characterized by $\nu = 4$ is destroyed by perturbations preserving the relevant symmetry. The above results indicate the emergence of the non-Hermitian $\mathbb{Z}_4$ skin effect protected by glide symmetry.

In Hermitian systems, it is known that glide symmetry results in Möbius surface states. The effects of glide symmetry on skin modes are left as a future work to be addressed.

ACKNOWLEDGMENTS

The authors thank Manfred Sigrist, Shu Hamanaka, and Tsugumi Matsumoto for fruitful discussions. This work is supported by JSPS KAKENHI Grants No. JP21K13850 and No. JP23KK0247 and JSPS Bilateral Program No. JPJSBP120249925. T.Y. is grateful for the support from the ETH Pauli Center for Theoretical Studies and a Grant from the Yamada Science Foundation.

APPENDIX A: $\mathbb{Z}_4$ TOPOLOGY IN HERMITIAN SYSTEMS

1. Symmetry constraints on Hermitian Hamiltonians

The symmetry class of the Hermitian Hamiltonian defined in Eq. (3) is the class DIII because it preserves the time-reversal symmetry (TRS) with Θ, the particle-hole symmetry (PHS) with C, and the chiral symmetry (CS) with Γ:

$$\Theta\tilde{H}(\boldsymbol{k})\Theta^{-1} = \tilde{H}(-\boldsymbol{k}), \tag{A1}$$

$$C\tilde{H}(\boldsymbol{k})C^{-1} = -\tilde{H}(-\boldsymbol{k}), \tag{A2}$$

$$\Gamma\tilde{H}(\boldsymbol{k})\Gamma^{-1} = -\tilde{H}(\boldsymbol{k}). \tag{A3}$$

Here, each of these symmetry operators is represented as $\Theta = \left(\begin{smallmatrix} 0 & \mathcal{T} \\ \mathcal{T} & 0 \end{smallmatrix}\right)\mathcal{K}$, $C = \left(\begin{smallmatrix} 0 & \mathcal{T} \\ -\mathcal{T} & 0 \end{smallmatrix}\right)\mathcal{K}$, and $\Gamma = \left(\begin{smallmatrix} 1 & 0 \\ 0 & -1 \end{smallmatrix}\right)$. Operator $\mathcal{K}$ takes complex conjugation. The glide symmetry is written as

$$G(k_x)\tilde{H}(\boldsymbol{k})G^{-1}(k_x) = \tilde{H}(\boldsymbol{k}), \tag{A4}$$

with

$$G(k_x) = \begin{pmatrix} 0 & \mathcal{G}(k_x) \\ \mathcal{G}(k_x) & 0 \end{pmatrix}, \tag{A5}$$

satisfying $\{G(k_x), \Theta C\} = 0$, $\Theta G(k_x) = G(-k_x)\Theta$, and $CG(k_x) = -G(-k_x)C$. We note that the relation $\Theta G(k_x) = G(-k_x)\Theta$ leads to $\mathcal{T}\mathcal{G}^*(k_x)\mathcal{T}^{-1} = \mathcal{G}(-k_x)$.

2. Hermitian Hamiltonians of $\nu = 1$, 2, and 4 and non-Hermitian toy models [Eqs. (5), (7), and (9)]

The doubled Hermitian Hamiltonian of $\nu = 1$ for the toy model defined in Eq. (5) is given by imposing glide symmetry on the Bernevig-Hughes-Zhang (BHZ) model [3,32]:

$$\begin{aligned} H_{\mathrm{BHZ}}(k_x, k_y) = {} & [m - 2t(\cos k_x + \cos k_y)]\tau_z s_0 \\ & + 2t_{\mathrm{sp}} \sin k_x \tau_y s_0 \\ & - 2t_{\mathrm{sp}} \sin k_y \tau_x s_z. \end{aligned} \tag{A6}$$

Here, m, t, and t_{sp} are real numbers. Pauli matrices are denoted by τ_i and s_i ($i = x$, y, and z); τ's act on the orbital space and s's act on the spin space. Corresponding identity matrices are denoted by τ_0 and s_0. Adding a staggered modulation of the lattice in the x direction and performing the unitary transformation, we obtain

$$\begin{aligned} & \tilde{H}_1(k_x, k_y) \\ & = [(m - 2t\cos k_y)\eta_0 - t\{(1 + \cos k_x)\eta_x - \sin k_x \eta_y\}]\tau_z s_0 \\ & \quad + t_{\mathrm{sp}}[\sin k_x \eta_x - (1 - \cos k_x)\eta_y]\tau_y s_0 \\ & \quad - 2t_{\mathrm{sp}} \sin k_y \eta_0 \tau_x s_z, \end{aligned} \tag{A7}$$

where η_i ($i = x$, y, and z) and η_0 are Pauli matrices and the identity matrix acting on the two inequivalent sites, respectively. The symmetry class of the Hermitian Hamiltonian $\tilde{H}_1$ is class DIII since it preserves TRS [Eq. (A1)] with $\Theta = i\eta_0\tau_0 s_y\mathcal{K}$, PHS [Eq. (A2)] with $C = \eta_0\tau_x s_0\mathcal{K}$, and CS [Eq. (A3)] with $\Gamma = \eta_0\tau_x s_y$. $\tilde{H}_1$ also satisfies the glide symmetry [Eq. (A4)] with $G(k_x) = i\left(\begin{smallmatrix} 0 & 1 \\ e^{-ik_x} & 0 \end{smallmatrix}\right)_\eta \tau_0 s_z$. If we choose the basis such that CS is represented as $\Gamma = \rho_0\chi_z$ where ρ's and χ's are Pauli matrices, $\tilde{H}_1$ is written as

$$\tilde{H}_1(k_x, k_y) = \begin{pmatrix} 0 & H_1(k_x, k_y) \\ H_1^\dagger(k_x, k_y) & 0 \end{pmatrix}_\chi. \tag{A8}$$

This Hamiltonian is the doubled Hermitian Hamiltonian with $E_{\mathrm{ref}} = 0$ for the toy model defined in Eq. (5).

The doubled Hermitian Hamiltonian of $\nu = 2$ for the toy model [Eq. (7)] is given by adding TRS to the following Hamiltonian which is constructed from spinless chiral p-wave superconductors on the square lattice [32]:

$$\begin{aligned} H_{e_+-e_-}(k_x, k_y) = {} & (m - t\cos k_y)\eta_0\tau_z \\ & + \kappa \sin(k_x/2)[\cos(k_x/2)\eta_x + \sin(k_x/2)\eta_y]\tau_x \\ & + \Delta \sin k_y \eta_0 \tau_y. \end{aligned} \tag{A9}$$

Here, t, κ, and Δ are real numbers. Pauli matrices are denoted by τ_i and η_i ($i = x$, y, and z); τ's act on the Nambu space and η's act on the sublattice space. Adding TRS to this Hamiltonian by using the freedom of the spin space, we obtain

$$\begin{aligned} \tilde{H}_2(k_x, k_y) = {} & (m - t\cos k_y)\eta_0\tau_z s_0 \\ & + \kappa \sin(k_x/2)[\cos(k_x/2)\eta_x + \sin(k_x/2)\eta_y]\tau_x s_z \\ & + \Delta \sin k_y \eta_0 \tau_y s_0 + 2\alpha \sin k_y \eta_z \tau_x s_x. \end{aligned} \tag{A10}$$

Here, s_i ($i = x$, y, and z) are Pauli matrices in the spin space. When the real number α is 0, the non-Hermitian Hamiltonian is decomposed into Hatano-Nelson models; $H_2(k_x, k_y)$ [Eq. (A12)] is written as

$$H_2(k_x, k_y) = m\eta_0\rho_0 + \begin{pmatrix} H^{(\mathrm{HN})}(k_y)\eta_0 & 0 \\ 0 & H^{(\mathrm{HN})}(-k_y)\eta_0 \end{pmatrix}_\rho, \tag{A11}$$

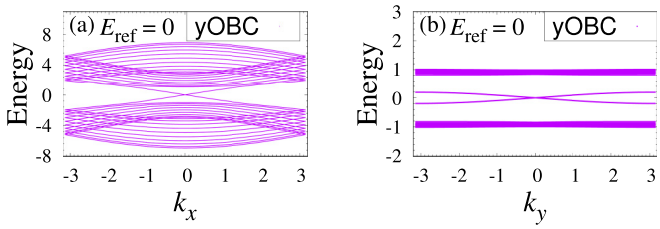

FIG. 7. (a) Energy spectra of the doubled Hamiltonian constructed from Eq. (5) under yOBC for $(L, m, t, t_{\rm sp}) = (10, 3, 1, 0.8)$ and $k_x = -\pi + 2\pi n/10^3 (n = 1, \ldots, 10^3)$. (b) Energy spectra of the doubled Hamiltonian constructed from Eq. (7) under yOBC for $(m, t, \kappa, \Delta, \alpha) = (0, 1, 0.2, 0.8, 0.1)$ and $k_x = -\pi + 2\pi n/10^3 (n = 1, \ldots, 10^3)$. These data are obtained by supposing that $L = 10$ unit cells are aligned in the y direction.

at $k_x = 0$. Here, $H^{(\rm HN)}(k) \equiv -t\cos k + i\Delta \sin k$ is the Hatano-Nelson model [42,43], which belongs to class A and can exhibit the NHSE characterized by a $\mathbb{Z}$ invariant. The Hamiltonian $\tilde{H}_2$ belongs to class DIII and satisfies the glide symmetry. The representation of each symmetry operator is the same as that in the case of $\tilde{H}_1$. If we choose the basis such that CS is represented as $\Gamma = \rho_0 \chi_z$ where ρ's and χ's are Pauli matrices, $\tilde{H}_2$ is written as

$$\tilde{H}_2(k_x, k_y) = \begin{pmatrix} 0 & H_2(k_x, k_y) \\ H_2^\dagger(k_x, k_y) & 0 \end{pmatrix}_\chi. \tag{A12}$$

This Hamiltonian is the doubled Hermitian Hamiltonian with $E_{\rm ref} = 0$ for the toy model defined in Eq. (7).

APPENDIX B: EDGE MODES OF THE DOUBLED HERMITIAN HAMILTONIAN

In Sec. II, the NHSE is observed at a specific wave number (i.e., $k_x = 0$) for the Hamiltonian whose $\mathbb{Z}_4$ invariant takes $\nu = 1$ and 2. This behavior is explained in terms of exact zero modes [62].

Figure 7(a) [Fig. 7(b)] shows the energy spectrum for the doubled Hermitian Hamiltonian constructed from Eq. (5) [Eq. (7)] under yOBC. These edge modes become zero modes at $k_x = 0$. The same result is obtained when the $E_{\rm ref}$ equals the eigenenergy of the skin mode. These results are consistent with the correspondence between the right eigenstates of the non-Hermitian Hamiltonian H and the edge modes of the doubled Hermitian Hamiltonian $\tilde{H}$. That is, the appearance of $|E_{\rm ref}\rangle$ satisfying $H|E_{\rm ref}\rangle = E_{\rm ref}|E_{\rm ref}\rangle$ under yOBC implies the existence of boundary modes $(0, |E_{\rm ref}\rangle)^T_\chi$ satisfying $\tilde{H}(0, |E_{\rm ref}\rangle)^T_\chi = 0$. The NHSE is not observed for $k_x \neq 0$ because of the absence of zero modes in $\tilde{H}$.

The argument of the doubled Hermitian Hamiltonian explains the destruction of the NHSE. Figure 8 shows the energy spectra of the doubled Hermitian Hamiltonian constructed from Eq. (9) under yOBC. For $\lambda \leqslant 0.2$, there are zero modes at specific wave numbers [see Figs. 8(a) and 8(b)] in which the NHSE for Eq. (9) are observed. On the other hand, for $\lambda > 0.2$ such that $\lambda = 0.3$, the zero modes disappear [see Fig. 8(c)]. This result is consistent with the disappearance of the NHSE for Eq. (9) when $\lambda > 0.2$.

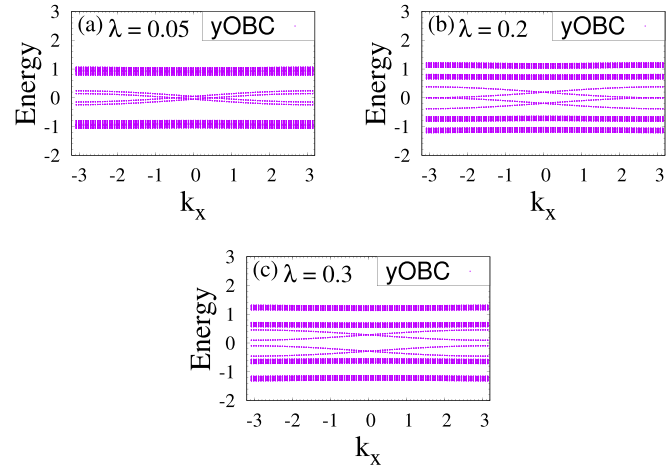

FIG. 8. (a)–(c) Energy spectra of the doubled Hamiltonian constructed from H_4 [see Eq. (9)] under yOBC for $\lambda = 0.05$, 0.2, and 0.3. These data are obtained for $(m, t, \kappa, \Delta, \alpha, E_{\rm ref}) = (0, 1, 0.2, 0.8, 0.1, 0)$ and $k_x = -\pi + 2\pi n/10^2 (n = 1, \ldots, 10^2)$. These data are obtained by supposing that $L = 10$ unit cells are aligned in the y direction.

APPENDIX C: TOPOLOGICAL INVARIANT FOR CLASS AII†

In Sec. III B, we consider the Hamiltonian defined in Eq. (7) which belongs to the symmetry class AII† and has glide symmetry added. The subsystem at $k_x = 0$ [i.e., $H_2'(k_y) \equiv H_2(0, k_y)$] belongs to the one-dimensional class AII† which is characterized by the following $\mathbb{Z}_2$ invariant [48,94–96], $\theta(E_{\rm ref}) \in \{0, 1\}$:

$$(-1)^{\theta(E_{\rm ref})} \equiv \mathrm{sgn}\left\{ \frac{\mathrm{Pf}[(H_2'(\pi) - E_{\rm ref})\mathcal{T}]}{\mathrm{Pf}[(H_2'(0) - E_{\rm ref})\mathcal{T}]} \times \exp\left[-\frac{1}{2} \int_{k=0}^{k=\pi} d \log\det [H_2'(k) - E_{\rm ref}]\mathcal{T} \right] \right\} \tag{C1}$$

We can compute numerically $\theta(E_{\rm ref})$ for $H_2'(k_y)$ and confirm that θ takes 0 $[\theta(E_{\rm ref}) = 0]$ for the parameter values used in Sec. III B if we set $E_{\rm ref}$ to the eigenenergy of the skin mode.

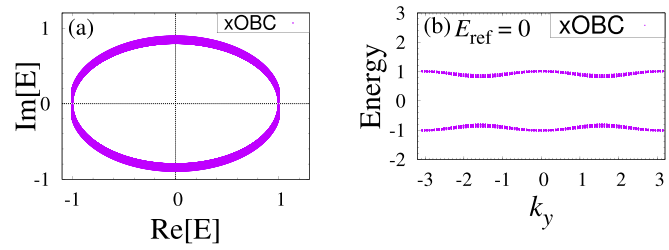

FIG. 9. (a) Energy spectra of H_2 [Eq. (7)] under xOBC for $k_y = 2\pi n/10^3 (n = 0, \ldots, 10^3 - 1)$. (b) Energy spectra of the doubled Hamiltonian constructed from Eq. (7) under xOBC for $k_y = -\pi + 2\pi n/10^2 (n = 1, \ldots, 10^2)$ and $E_{\rm ref} = 0$. These data are obtained by supposing that $L = 10$ unit cells are aligned in the x direction and for $(m, t, \kappa, \Delta, \alpha) = (0, 1.0, 0.2, 0.8, 10^{-1})$.

This result is understood as follows: the subsystem at $k_x = 0$ can be regarded as two copies of a one-dimensional system with $\theta(E_{\rm ref}) = 1$ [see Eq. (A11)]. Thus, in total we have $\theta(E_{\rm ref}) = 2 = 0\,(\mathrm{mod}\,2)$ for $H_2'(k_y)$.

APPENDIX D: SPECTRUM AND EIGENSTATES UNDER xOBC and yPBC

If we impose the xOBC, the glide symmetry is not closed because the glide operation involves the translation by half a lattice constant in the x direction. In this case, the NHSE is not observed for Hamiltonian Eq. (7).

We compute the energy spectrum under xOBC and yPBC [see Fig. 9(a)]. Figure 9(a) shows that the energy spectrum exists away from the real axis, which is similar to the case of xPBC and yPBC. Thus, the NHSE disappears when the glide symmetry is not closed. This result implies that the NHSE for $\nu = 2$ is protected by the glide symmetry. Besides, we confirm that the edge modes do not appear for the doubled Hamiltonian constructed from Eq. (7) under xOBC and yPBC [see Fig. 9(b)].

[1] C. L. Kane and E. J. Mele, Quantum spin Hall effect in graphene, Phys. Rev. Lett. **95**, 226801 (2005).

[2] C. L. Kane and E. J. Mele, Z_2 topological order and the quantum spin Hall effect, Phys. Rev. Lett. **95**, 146802 (2005).

[3] B. A. Bernevig, T. L. Hughes, and S.-C. Zhang, Quantum spin Hall effect and topological phase transition in HgTe quantum wells, Science **314**, 1757 (2006).

[4] X.-L. Qi, T. L. Hughes, and S.-C. Zhang, Topological field theory of time-reversal invariant insulators, Phys. Rev. B **78**, 195424 (2008).

[5] M. Z. Hasan and C. L. Kane, Colloquium: Topological insulators, Rev. Mod. Phys. **82**, 3045 (2010).

[6] X.-L. Qi and S.-C. Zhang, Topological insulators and superconductors, Rev. Mod. Phys. **83**, 1057 (2011).

[7] K. v. Klitzing, G. Dorda, and M. Pepper, New method for high-accuracy determination of the fine-structure constant based on quantized Hall resistance, Phys. Rev. Lett. **45**, 494 (1980).

[8] B. I. Halperin, Quantized Hall conductance, current-carrying edge states, and the existence of extended states in a two-dimensional disordered potential, Phys. Rev. B **25**, 2185 (1982).

[9] D. J. Thouless, M. Kohmoto, M. P. Nightingale, and M. den Nijs, Quantized Hall conductance in a two-dimensional periodic potential, Phys. Rev. Lett. **49**, 405 (1982).

[10] J. E. Avron, R. Seiler, and B. Simon, Homotopy and quantization in condensed matter physics, Phys. Rev. Lett. **51**, 51 (1983).

[11] Y. Hatsugai, Edge states in the integer quantum Hall effect and the Riemann surface of the Bloch function, Phys. Rev. B **48**, 11851 (1993).

[12] Y. Hatsugai, Chern number and edge states in the integer quantum Hall effect, Phys. Rev. Lett. **71**, 3697 (1993).

[13] V. P. Gusynin and S. G. Sharapov, Unconventional integer quantum Hall effect in graphene, Phys. Rev. Lett. **95**, 146801 (2005).

[14] W. P. Su, J. R. Schrieffer, and A. J. Heeger, Soliton excitations in polyacetylene, Phys. Rev. B **22**, 2099 (1980).

[15] A. Altland and M. R. Zirnbauer, Nonstandard symmetry classes in mesoscopic normal-superconducting hybrid structures, Phys. Rev. B **55**, 1142 (1997).

[16] A. Y. Kitaev, Unpaired Majorana fermions in quantum wires, Phys.-Usp. **44**, 131 (2001).

[17] L. Fu and C. L. Kane, Time reversal polarization and a Z_2 adiabatic spin pump, Phys. Rev. B **74**, 195312 (2006).

[18] A. P. Schnyder, S. Ryu, A. Furusaki, and A. W. W. Ludwig, Classification of topological insulators and superconductors in three spatial dimensions, Phys. Rev. B **78**, 195125 (2008).

[19] A. Kitaev, Periodic table for topological insulators and superconductors, AIP Conf. Proc. **1134**, 22 (2009).

[20] S. Ryu, A. P. Schnyder, A. Furusaki, and A. W. W. Ludwig, Topological insulators and superconductors: Tenfold way and dimensional hierarchy, New J. Phys. **12**, 065010 (2010).

[21] C.-K. Chiu, J. C. Y. Teo, A. P. Schnyder, and S. Ryu, Classification of topological quantum matter with symmetries, Rev. Mod. Phys. **88**, 035005 (2016).

[22] J. C. Y. Teo, L. Fu, and C. L. Kane, Surface states and topological invariants in three-dimensional topological insulators: Application to $Bi_{1-x}Sb_x$, Phys. Rev. B **78**, 045426 (2008).

[23] L. Fu, Topological crystalline insulators, Phys. Rev. Lett. **106**, 106802 (2011).

[24] T. H. Hsieh, H. Lin, J. Liu, W. Duan, A. Bansil, and L. Fu, Topological crystalline insulators in the SnTe material class, Nat. Commun. **3**, 982 (2012).

[25] Y. Tanaka, R. Zhi, T. Sato, K. Nakayama, S. Souma, T. Takahashi, K. Segawa, and Y. Ando, Experimental realization of a topological crystalline insulator in SnTe, Nat. Phys. **8**, 800 (2012).

[26] C.-K. Chiu, H. Yao, and S. Ryu, Classification of topological insulators and superconductors in the presence of reflection symmetry, Phys. Rev. B **88**, 075142 (2013).

[27] T. Morimoto and A. Furusaki, Topological classification with additional symmetries from Clifford algebras, Phys. Rev. B **88**, 125129 (2013).

[28] K. Shiozaki and M. Sato, Topology of crystalline insulators and superconductors, Phys. Rev. B **90**, 165114 (2014).

[29] C.-X. Liu, R.-X. Zhang, and B. K. VanLeeuwen, Topological nonsymmorphic crystalline insulators, Phys. Rev. B **90**, 085304 (2014).

[30] K. Shiozaki, M. Sato, and K. Gomi, Z_2 topology in nonsymmorphic crystalline insulators: Möbius twist in surface states, Phys. Rev. B **91**, 155120 (2015).

[31] C. Fang and L. Fu, New classes of three-dimensional topological crystalline insulators: Nonsymmorphic and magnetic, Phys. Rev. B **91**, 161105(R) (2015).

[32] K. Shiozaki, M. Sato, and K. Gomi, Topology of nonsymmorphic crystalline insulators and superconductors, Phys. Rev. B **93**, 195413 (2016).

[33] Z. Wang, A. Alexandradinata, R. J. Cava, and B. A. Bernevig, Hourglass fermions, Nature (London) **532**, 189 (2016).

[34] L. M. Schoop, M. N. Ali, C. Straßer, A. Topp, A. Varykhalov, D. Marchenko, V. Duppel, S. S. P. Parkin, B. V. Lotsch, and C. R. Ast, Dirac cone protected by non-symmorphic symmetry and three-dimensional Dirac line node in ZrSiS, Nat. Commun. **7**, 11696 (2016).

[35] Y. X. Zhao and A. P. Schnyder, Nonsymmorphic symmetry-required band crossings in topological semimetals, Phys. Rev. B **94**, 195109 (2016).
[36] J. Kruthoff, J. de Boer, J. van Wezel, C. L. Kane, and R.-J. Slager, Topological classification of crystalline insulators through band structure combinatorics, Phys. Rev. X **7**, 041069 (2017).
[37] J. Ma, C. Yi, B. Lv, Z. Wang, S. Nie, L. Wang, L. Kong, Y. Huang, P. Richard, P. Zhang, K. Yaji, K. Kuroda, S. Shin, H. Weng, B. A. Bernevig, Y. Shi, T. Qian, and H. Ding, Experimental evidence of hourglass fermion in the candidate nonsymmorphic topological insulator KHgSb, Sci. Adv. **3**, e1602415 (2017).
[38] C. Zhang, Z. Y. Chen, Z. Zhang, and Y. X. Zhao, General theory of momentum-space nonsymmorphic symmetry, Phys. Rev. Lett. **130**, 256601 (2023).
[39] M. Tymczyszyn and E. McCann, One-dimensional $\mathbb{Z}_4$ topological superconductor, Phys. Rev. B **110**, 085416 (2024).
[40] A. Daido, T. Yoshida, and Y. Yanase, $\mathbb{Z}_4$ topological superconductivity in UCoGe, Phys. Rev. Lett. **122**, 227001 (2019).
[41] P.-Y. Chang, O. Erten, and P. Coleman, Möbius Kondo insulators, Nat. Phys. **13**, 794 (2017).
[42] N. Hatano and D. R. Nelson, Localization transition in non-Hermitian quantum mechanics, Phys. Rev. Lett. **77**, 570 (1996).
[43] N. Hatano and D. R. Nelson, Vortex pinning and non-Hermitian quantum mechanics, Phys. Rev. B **56**, 8651 (1997).
[44] Y. C. Hu and T. L. Hughes, Absence of topological insulator phases in non-Hermitian PT-symmetric Hamiltonians, Phys. Rev. B **84**, 153101 (2011).
[45] K. Esaki, M. Sato, K. Hasebe, and M. Kohmoto, Edge states and topological phases in non-Hermitian systems, Phys. Rev. B **84**, 205128 (2011).
[46] T. E. Lee, Anomalous edge state in a non-Hermitian lattice, Phys. Rev. Lett. **116**, 133903 (2016).
[47] Z. Gong, Y. Ashida, K. Kawabata, K. Takasan, S. Higashikawa, and M. Ueda, Topological phases of non-Hermitian systems, Phys. Rev. X **8**, 031079 (2018).
[48] K. Kawabata, K. Shiozaki, M. Ueda, and M. Sato, Symmetry and topology in non-Hermitian physics, Phys. Rev. X **9**, 041015 (2019).
[49] Y. Ashida, Z. Gong, and M. Ueda, Non-Hermitian physics, Adv. Phys. **69**, 249 (2020).
[50] E. J. Bergholtz, J. C. Budich, and F. K. Kunst, Exceptional topology of non-Hermitian systems, Rev. Mod. Phys. **93**, 015005 (2021).
[51] N. Okuma and M. Sato, Non-Hermitian topological phenomena: A review, Annu. Rev. Condens. Matter Phys. **14**, 83 (2023).
[52] R. Lin, T. Tai, L. Li, and C. H. Lee, Topological non-Hermitian skin effect, Front. Phys. **18**, 53605 (2023).
[53] S. Manna and B. Roy, Inner skin effects on non-Hermitian topological fractals, Commun. Phys. **6**, 10 (2023).
[54] F. K. Kunst, E. Edvardsson, J. C. Budich, and E. J. Bergholtz, Biorthogonal bulk-boundary correspondence in non-Hermitian systems, Phys. Rev. Lett. **121**, 026808 (2018).
[55] K. Yokomizo and S. Murakami, Non-Bloch band theory of non-Hermitian systems, Phys. Rev. Lett. **123**, 066404 (2019).
[56] H. Shen, B. Zhen, and L. Fu, Topological band theory for non-Hermitian Hamiltonians, Phys. Rev. Lett. **120**, 146402 (2018).
[57] V. Kozii and L. Fu, Non-Hermitian topological theory of finite-lifetime quasiparticles: Prediction of bulk Fermi arc due to exceptional point, Phys. Rev. B **109**, 235139 (2024).
[58] T. Yoshida, R. Peters, and N. Kawakami, Non-Hermitian perspective of the band structure in heavy-fermion systems, Phys. Rev. B **98**, 035141 (2018).
[59] S. Yao and Z. Wang, Edge states and topological invariants of non-Hermitian systems, Phys. Rev. Lett. **121**, 086803 (2018).
[60] S. Yao, F. Song, and Z. Wang, Non-Hermitian Chern bands, Phys. Rev. Lett. **121**, 136802 (2018).
[61] C. H. Lee and R. Thomale, Anatomy of skin modes and topology in non-Hermitian systems, Phys. Rev. B **99**, 201103(R) (2019).
[62] N. Okuma, K. Kawabata, K. Shiozaki, and M. Sato, Topological origin of non-Hermitian skin effects, Phys. Rev. Lett. **124**, 086801 (2020).
[63] D. S. Borgnia, A. J. Kruchkov, and R.-J. Slager, Non-Hermitian boundary modes and topology, Phys. Rev. Lett. **124**, 056802 (2020).
[64] K. Zhang, Z. Yang, and C. Fang, Correspondence between winding numbers and skin modes in non-Hermitian systems, Phys. Rev. Lett. **125**, 126402 (2020).
[65] X. Zhang, T. Zhang, M.-H. Lu, and Y.-F. Chen, A review on non-Hermitian skin effect, Adv. Phys.: X **7**, 2109431 (2022).
[66] T. Yoshida, T. Mizoguchi, and Y. Hatsugai, Mirror skin effect and its electric circuit simulation, Phys. Rev. Res. **2**, 022062(R) (2020).
[67] T. Hofmann, T. Helbig, F. Schindler, N. Salgo, M. Brzezińska, M. Greiter, T. Kiessling, D. Wolf, A. Vollhardt, A. Kabaši, C. H. Lee, A. Bilušić, R. Thomale, and T. Neupert, Reciprocal skin effect and its realization in a topolectrical circuit, Phys. Rev. Res. **2**, 023265 (2020).
[68] T. Helbig, T. Hofmann, S. Imhof, M. Abdelghany, T. Kiessling, L. W. Molenkamp, C. H. Lee, A. Szameit, M. Greiter, and R. Thomale, Generalized bulk-boundary correspondence in non-Hermitian topolectrical circuits, Nat. Phys. **16**, 747 (2020).
[69] S. Liu, R. Shao, S. Ma, L. Zhang, O. You, H. Wu, Y. J. Xiang, T. J. Cui, and S. Zhang, Non-Hermitian skin effect in a non-Hermitian electrical circuit, Research **2021**, 5608038 (2021).
[70] D. Zou, T. Chen, W. He, J. Bao, C. H. Lee, H. Sun, and X. Zhang, Observation of hybrid higher-order skin-topological effect in non-Hermitian topolectrical circuits, Nat. Commun. **12**, 7201 (2021).
[71] X. Zhang, Y. Tian, J.-H. Jiang, M.-H. Lu, and Y.-F. Chen, Observation of higher-order non-Hermitian skin effect, Nat. Commun. **12**, 5377 (2021).
[72] C. Shang, S. Liu, R. Shao, P. Han, X. Zang, X. Zhang, K. N. Salama, W. Gao, C. H. Lee, R. Thomale, A. Manchon, S. Zhang, T. J. Cui, and U. Schwingenschlögl, Experimental identification of the second-order non-Hermitian skin effect with physics-graph-informed machine learning, Adv. Sci. **9**, 2202922 (2022).
[73] L. Zhang, Y. Yang, Y. Ge, Y.-J. Guan, Q. Chen, Q. Yan, F. Chen, R. Xi, Y. Li, D. Jia, S.-Q. Yuan, H.-X. Sun, H. Chen, and B. Zhang, Acoustic non-Hermitian skin effect from twisted winding topology, Nat. Commun. **12**, 6297 (2021).
[74] H. Zhang, T. Chen, L. Li, C. H. Lee, and X. Zhang, Electrical circuit realization of topological switching for the non-Hermitian skin effect, Phys. Rev. B **107**, 085426 (2023).

[75] S. Weidemann, M. Kremer, T. Helbig, T. Hofmann, A. Stegmaier, M. Greiter, R. Thomale, and A. Szameit, Topological funneling of light, Science **368**, 311 (2020).

[76] Y. Song, W. Liu, L. Zheng, Y. Zhang, B. Wang, and P. Lu, Two-dimensional non-Hermitian skin effect in a synthetic photonic lattice, Phys. Rev. Appl. **14**, 064076 (2020).

[77] L. Xiao, T. Deng, K. Wang, Z. Wang, W. Yi, and P. Xue, Observation of non-Bloch parity-time symmetry and exceptional points, Phys. Rev. Lett. **126**, 230402 (2021).

[78] K. Wang, T. Li, L. Xiao, Y. Han, W. Yi, and P. Xue, Detecting non-Bloch topological invariants in quantum dynamics, Phys. Rev. Lett. **127**, 270602 (2021).

[79] M. Brandenbourger, X. Locsin, E. Lerner, and C. Coulais, Non-reciprocal robotic metamaterials, Nat. Commun. **10**, 4608 (2019).

[80] A. Ghatak, M. Brandenbourger, J. van Wezel, and C. Coulais, Observation of non-Hermitian topology and its bulk-edge correspondence in an active mechanical metamaterial, Proc. Natl. Acad. Sci. USA **117**, 29561 (2020).

[81] A. Wang, Z. Meng, and C. Q. Chen, Non-Hermitian topology in static mechanical metamaterials, Sci. Adv. **9**, eadf7299 (2023).

[82] W. Gou, T. Chen, D. Xie, T. Xiao, T.-S. Deng, B. Gadway, W. Yi, and B. Yan, Tunable nonreciprocal quantum transport through a dissipative Aharonov-Bohm ring in ultracold atoms, Phys. Rev. Lett. **124**, 070402 (2020).

[83] L. Xiao, T. Deng, K. Wang, G. Zhu, Z. Wang, W. Yi, and P. Xue, Non-Hermitian bulk-boundary correspondence in quantum dynamics, Nat. Phys. **16**, 761 (2020).

[84] L. S. Palacios, S. Tchoumakov, M. Guix, I. Pagonabarraga, S. Sánchez, and A. G. Grushin, Guided accumulation of active particles by topological design of a second-order skin effect, Nat. Commun. **12**, 4691 (2021).

[85] Q. Liang, D. Xie, Z. Dong, H. Li, H. Li, B. Gadway, W. Yi, and B. Yan, Dynamic signatures of non-Hermitian skin effect and topology in ultracold atoms, Phys. Rev. Lett. **129**, 070401 (2022).

[86] R. Shen, T. Chen, B. Yang, and C. H. Lee, Observation of the non-Hermitian skin effect and Fermi skin on a digital quantum computer, arXiv:2311.10143.

[87] H. C. Wu, L. Jin, and Z. Song, Topology of an anti-parity-time symmetric non-Hermitian Su-Schrieffer-Heeger model, Phys. Rev. B **103**, 235110 (2021).

[88] Y. Tanaka, R. Takahashi, and R. Okugawa, Non-Hermitian skin effect enforced by nonsymmorphic symmetries, Phys. Rev. B **109**, 035131 (2024).

[89] J. L. K. König, F. Herber, and E. J. Bergholtz, Nodal phases in non-Hermitian wallpaper crystals, Appl. Phys. Lett. **124**, 051109 (2024).

[90] T. Fukui, Y. Hatsugai, and H. Suzuki, Chern numbers in discretized Brillouin zone: Efficient method of computing (spin) Hall conductances, J. Phys. Soc. Jpn. **74**, 1674 (2005).

[91] T. Fukui and Y. Hatsugai, Quantum spin Hall effect in three dimensional materials: Lattice computation of Z_2 topological invariants and its application to Bi and Sb, J. Phys. Soc. Jpn. **76**, 053702 (2007).

[92] T. Yoshida, A. Daido, N. Kawakami, and Y. Yanase, Efficient method to compute $\mathbb{Z}_4$ indices with glide symmetry and applications to the Möbius materials CeNiSn and UCoGe, Phys. Rev. B **99**, 235105 (2019).

[93] In the presence of TRS†, the skin modes localized around right and left edges are degenerated, which yields a numerical difficulty to capture skin modes. Thus, we have introduced a perturbation to lift this degeneracy.

[94] X.-L. Qi, T. L. Hughes, and S.-C. Zhang, Topological invariants for the Fermi surface of a time-reversal-invariant superconductor, Phys. Rev. B **81**, 134508 (2010).

[95] A. P. Schnyder and S. Ryu, Topological phases and surface flat bands in superconductors without inversion symmetry, Phys. Rev. B **84**, 060504(R) (2011).

[96] J. C. Budich and E. Ardonne, Topological invariant for generic one-dimensional time-reversal-symmetric superconductors in class DIII, Phys. Rev. B **88**, 134523 (2013).